

## RESEARCH ARTICLE

10.1029/2018JB015883

## Key Points:

- The linear approximation in the modeled relationship between gravity and topography is removed
- Estimate using gravity gradients which are more sensitive to topography at short wavelengths
- Estimation accuracy in rugged areas is improved by modeling the nonlinearities

## Correspondence to:

J. Yang and C. Jekeli,  
 yang.741@osu.edu;  
 jekeli.1@osu.edu

## Citation:

Yang, J., Jekeli, C., & Liu, L. (2018). Seafloor topography estimation from gravity gradients using simulated annealing. *Journal of Geophysical Research: Solid Earth*, 123, 6958–6975. <https://doi.org/10.1029/2018JB015883>

Received 1 APR 2018

Accepted 21 JUN 2018

Accepted article online 28 JUN 2018

Published online 11 AUG 2018

# Seafloor Topography Estimation From Gravity Gradients Using Simulated Annealing

 Junjun Yang<sup>1</sup> , Christopher Jekeli<sup>2</sup> , and Lintao Liu<sup>3</sup>

<sup>1</sup>Institute of Geophysics, MOE Key Laboratory of Fundamental Physical Quantities Measurement, School of Physics, Huazhong University of Science and Technology, Wuhan, China, <sup>2</sup>Division of Geodetic Science, School of Earth Sciences, The Ohio State University, Columbus, OH, USA, <sup>3</sup>State Key Laboratory of Geodesy and Earth's Dynamics, Institute of Geodesy and Geophysics, Chinese Academy of Sciences, Wuhan, China

**Abstract** Inferring seafloor topography from gravity anomaly currently is the dominant method to obtain a global view of the oceans. Standard techniques rely on an approximate, linear relationship between topography and gravity, which is valid only if the local topography is smooth compared with the regional topography, so the estimation accuracy in the very rugged areas is low. Current methods can be improved by removing the linear approximation and estimating the topography through simulated annealing and by using gravity gradiometry that is more sensitive to topography at short wavelengths than the gravity anomaly. Simulated annealing is a global optimization technique that can process nonlinear inverse problems. It is developed to estimate the seafloor depths by minimizing the difference between the observed and forward-computed vertical gravity gradients. The method is tested on altimetry-derived gravity gradients in a  $2^\circ \times 2^\circ$  area of rugged seafloor topography in the West Pacific Ocean and results in estimates with a root-mean-square error of  $\pm 236$  m. Compared to estimates from an existing model obtained by standard techniques this represents an accuracy improvement of 22%.

## 1. Introduction

The ocean covers 71% of the Earth's surface. However, our knowledge about the topography of the seafloor in some areas is even less than that of Mars because it is difficult to observe directly (Smith et al., 2001; Wieczorek, 2015). Searching for the recently missing Malaysia Airlines flight MH370 shows the difficulty in viewing the ocean bottom and how little we know about it (Smith & Marks, 2014). The ocean bottom requires more detailed mapping in order to exploit its ample natural resources and to obtain information for improved understanding in geophysics and geodynamics (ocean circulation, earthquakes, and volcanoes), as well as submarine navigation (Jakobsson, 2017).

Since the 1950s, the seafloor depth was measured by ship using single-beam echo sounders, and later in the 1980s the multibeam swath-mapping systems came into use (Smith & Sandwell, 1997). Although ship sounding provides high-resolution mapping, it is slow and expensive. A systematic mapping of the global ocean by this method would take more than 900 ship years (Sandwell et al., 2006; Smith & Sandwell, 2004; Weatherall et al., 2015). After 60 years of surveying, the ship sounding only covers about 18% of the ocean floor (Jakobsson, 2017; Weatherall et al., 2015).

Except for ship sounding, the seafloor topography can be indirectly inferred from gravity. It currently is the best way to obtain a global view, provided one has global gravity coverage. The fact that the gravity anomaly is correlated with topography is recognized already for over 200 years (Lewis & Dorman, 1970; McKenzie & Bowin, 1976; McNutt, 1979; Ribe, 1982; Watts, 1978). Analogous to land topography, seafloor topography contributes most to the short-to-medium wavelength components of the gravity anomaly while the long-wavelength components are partially isostatically compensated. Dixon et al. (1983) was one of the first to demonstrate the feasibility of inferring the seafloor topography through altimetry data (Sailor & Okal, 1983; White et al., 1983). Inspired by these early results, Smith and Sandwell (1994, 1997) estimated the seafloor topography based on gravity anomalies derived with  $\pm(3-5)$  mGal accuracy from the Seasat, Geosat, and ERS 1 satellite altimetry missions (Sandwell & Smith, 1992, 1997) and thus filled previously poorly charted areas. The global topography model (Sandwell et al., 2014; Smith & Sandwell, 1997), released by the Scripps Institution of Oceanography (SIO), has been incorporated into most publicly available global

seafloor topography models, such as DBDB2, ETOPO2, GINA, and the General Bathymetric Chart of the Oceans (Jakobsson et al., 2012; Marks & Smith, 2006; Marks et al., 2010; Weatherall et al., 2015). Hu et al. (2014) estimated the seafloor topography using vertical gravity gradients derived from satellite altimetry. Their method is similar to Smith and Sandwell's (1994) algorithm.

The techniques of Smith and Sandwell (1994, 1997) rely on an approximate, linear relationship between topography and gravity. In fact, it is a first-term approximation to Parker's theory (Parker, 1972), which is valid only if the local topography is small compared with the regional topography. Numerical analysis in section 2.2 shows that in rugged areas (topography ranges from  $-1$  to  $-5$  km over a 200 km by 200 km rectangular area), the nonlinear terrain effect for the vertical gravity gradient (VGG) can be as much as 49 Eötvös (see the discussion related to Figure 2). At wavelengths shorter than 5 km, more than half of the VGG derives from the nonlinear terms of Parker's infinite series. Therefore, it is important to consider nonlinear terms in the inversion process and this requires new algorithms that can handle tens of thousands of parameters in nonlinear models. Moreover, Smith and Sandwell's (1994, 1997) algorithms were developed in early 1990s. Development of the computer hardware in the past two decades now enables exploration of more computationally expensive approaches. These approaches may improve the estimation accuracy and thus enhance our knowledge of the seafloor. Last but not least, current methods have used altimetry-derived gravity anomalies to infer seafloor topography. Gravity gradients are more sensitive to the short-wavelength topography than gravity anomalies (Barnes et al., 2011), so the corresponding performance in topography prediction is expected to be better.

In the following sections, current methods are improved by removing the linear approximation in the modeled relationship between gravity and topography through a global optimization technique called simulated annealing. These improvements are important in updating the global seafloor model to achieve higher accuracy and resolution, which has not seen major improvement for more than 20 years.

## 2. Methods

### 2.1. Traditional Parker's Method

Parker's FFT-based (Fast Fourier Transform) method is a generalization of the technique used by Smith and Sandwell (1994, 1997) that makes use of the gravity gradients rather than the gravity anomalies. The gravity gradient is the combination of the topographic effect, isostatic compensation at the Mohorovicic discontinuity, and density variations within the Earth. The isostatic compensation mechanism is not considered here because its effect is mainly in the long wavelengths, whereas the topography estimation is limited to short-to-intermediate wavelengths. In addition, the density of the seafloor topography is assumed uniform throughout this study. The VGG at sea level,  $\Gamma_{zz}$ , generated by  $b_r$ , the local seafloor topography deviating from the mean sea depth  $d$  ( $b_r$  could be positive or negative while  $d$  is defined to be negative), is given by (Jekeli, 2017; Parker, 1972)

$$F(\Gamma_{zz}) = 2\pi G \Delta \rho e^{2\pi \tilde{f} d} \sum_{n=1}^{\infty} \frac{(2\pi \tilde{f})^n}{n!} F(b_r^n), \quad (1)$$

where  $F$  denotes the 2-D Fourier transform,  $G$  is the gravitational constant,  $\tilde{f} = \sqrt{f_x^2 + f_y^2}$  is radial frequency,  $f_x$  and  $f_y$  are cycle frequencies, and  $\Delta \rho = \rho_c - \rho_w$  is the density difference between the crust and sea water.

If the local topography is relatively small, the first term of the right-hand side of the infinite series is the dominant term (Parker, 1972):

$$F(\Gamma_{zz}) \approx 4\pi^2 \tilde{f} G \Delta \rho e^{2\pi \tilde{f} d} F(b_r) = Z_{\Gamma_{zz}}(\tilde{f}) F(b_r), \quad (2)$$

where  $Z_{\Gamma_{zz}}(\tilde{f})$  is called *gravity gradient admittance* and is shown in Figure 1.

Conversely, one could invert given VGG to obtain seafloor topography:

$$F(b_r) = Z_{\Gamma_{zz}}^{-1}(\tilde{f}) F(\Gamma_{zz}). \quad (3)$$

However, Figure 1 shows that at short and long wavelengths the VGG is less sensitive to the seafloor topography, due to the upward continuation operator  $e^{2\pi \tilde{f} d}$  and the  $-2\pi \tilde{f}$  factor in equation (2), respectively.

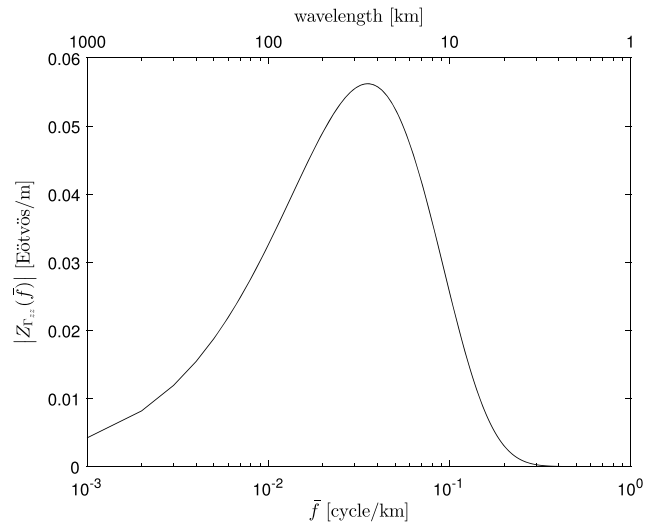


**Figure 1.** The theoretical gravity gradient admittance.  $d$  is set to  $-4.5$  km, and  $\Delta\rho$  is set to  $1.64$  g/cm<sup>3</sup>.

Therefore, estimating topography using gravity gradient is stable only in a certain short-to-medium wavelength band.

Rearranging equation (2), multiplying both sides by a band-pass filter  $W(\vec{f})$  and taking the inverse Fourier transform on both sides, we have

$$\mathcal{F}^{-1}[\mathcal{F}(b_r)W(\vec{f})] = (2\pi G\Delta\rho)^{-1}\mathcal{F}^{-1}[(2\pi\vec{f})^{-1}e^{-2\pi i\vec{f}d}\mathcal{F}(\Gamma_{zz})W(\vec{f})], \quad (4)$$

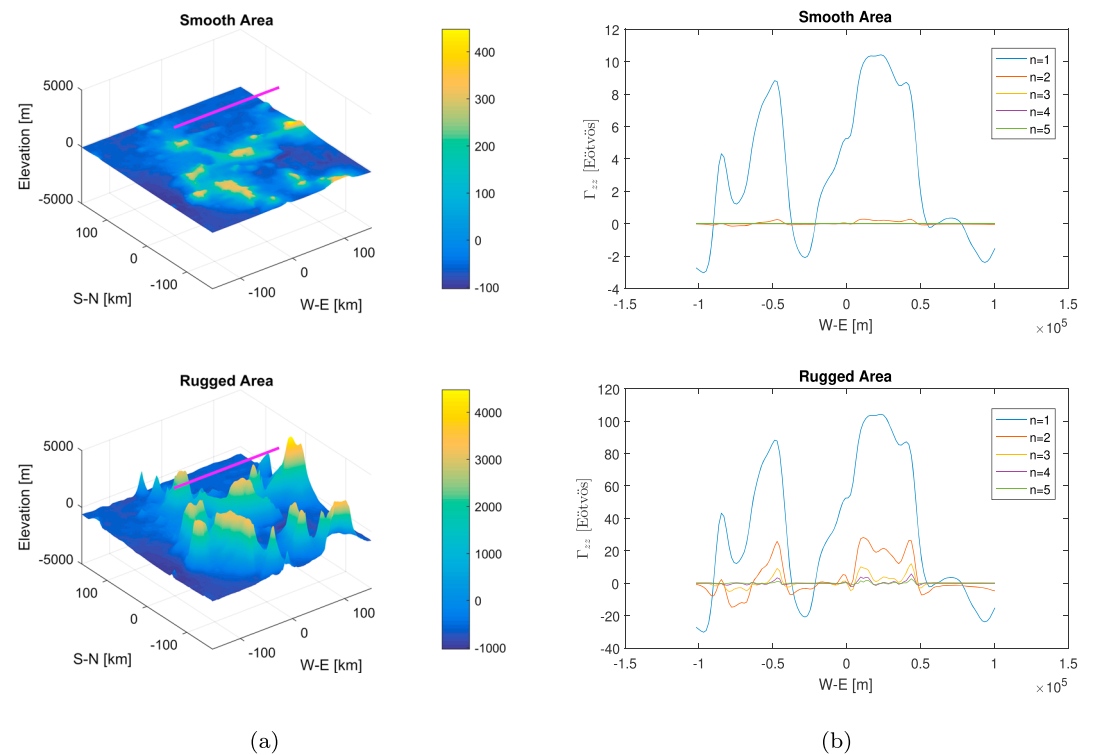


**Figure 2.** (a) Smooth and rugged simulated digital elevation models. The units of the color bars are meters. The magenta lines are the locations where the gravitational gradients are computed. (b) The first five terms of the series in (1) of the vertical gravitational gradient  $\Gamma_{zz}$  for the two areas.

where  $(2\pi\tilde{f})^{-1}e^{-2\pi\tilde{f}d}\mathcal{F}(\Gamma_{zz})$  may be called an *equivalent gravity anomaly*. Equation (4) indicates that when band-pass filtered and multiplied by a scaling factor, the equivalent gravity anomaly gives the intermediate wavelength component of the topography. The long-wavelength topography is obtained by low-pass filtering existing ship soundings. The sum of the intermediate and long-wavelength components gives the total predicted topography. The short wavelengths are omitted. They could only be obtained through multibeam echo sounders.

## 2.2. Analysis of the Nonlinear Terms

The traditional algorithm introduced in the last section is based on the assumption that the seafloor topography and the VGG are related by the first-term approximation in Parker's theory. In this section, the validity of this assumption is analyzed.

### 2.2.1. Numerical Analysis

To be specific, equation (1) describes the nonlinear relation between gravity gradient and seafloor topography. The linear term ( $n = 1$  term) in equation (1) was assumed to be dominant in the frequency domain inversion method (section 2.1), and the nonlinear terms ( $n > 1$  terms) negligible.  $b_r$  is the deviation of the actual topography from the reference plane  $z = d$ . The selection of this reference plane is entirely arbitrary because the VGG effect due to an infinite horizontal slab with uniform density is zero. Thus, one can choose the mean seafloor depth as the reference plane to obtain the fastest rate of convergence, that is, to let the series concentrate on the  $n = 1$  term. Since in the present case,  $|d| > \max|b_r|$ , the right-hand side of (1) converges (Parker, 1972). Moreover, Parker (1972) shows that the rate of convergence depends on the ratio,  $\frac{\max|b_r|}{|d|}$ , where a smaller value leads to a faster rate.

For a given  $d$ , if  $|b_r|$  is large, then neglecting the nonlinear terms can cause significant errors. Let us consider two areas with the same mean seafloor depth  $d$ : one smooth area with smaller  $\max|b_r|$ , and one rugged area with larger  $\max|b_r|$ . The digital elevation models (DEM) of a smooth and a rugged area were synthesized to analyze the dominance of the  $n = 1$  term; see Figure 2a. The simulated DEM for the rugged area is constructed using the bathymetric depth grid used in the discussion related to Figure 6b, so that the roughness of the simulated DEM is of the same order as the study area in section 3. Note that the seafloor depth  $b$  ( $b$  is always negative) has been transformed to the local seafloor topography with respect to the mean depth through  $b_r = b - d$ . In other words, the  $z$  axis origin has been translated from sea level to the mean depth to let the series concentrate on the  $n = 1$  term. The DEM of the smooth area is built in the same way, except that the magnitude of topographic height is divided by 10. The vertical gravitational gradients at constant altitude  $z = 4530.3$  m and above the center of each area are computed through equation (1), with computation results shown in Figure 2b.

Figure 2b clearly shows that in the smooth area, the  $n = 1$  term of Parker's series is dominant and the nonlinear terms are small, whereas in the rugged area the nonlinear terms are not negligible compared to the  $n = 1$  term. The total VGG is computed through equation (1), using the first 16 terms for the smooth area and the first 49 terms for the rugged area. Higher-order terms are neglected because they are smaller than the computer precision. The largest difference between the total VGG and the linear term is 0.3 Eötvös in the smooth area, whereas it is as large as 48.9 Eötvös in the rugged area.

### 2.2.2. Algorithmic Analysis Through Radially Symmetric Coherency

An alternative more algorithmic approach, called coherency analysis, can be used to examine the linearity between gravity gradient and topography.

The *coherency*, also called *magnitude squared coherence*, is defined as the square of the normalized cross-Power-Spectral-Density (PSD), so that it is in the interval between zero and unity for all frequencies. The coherency between 1-D signals  $\Gamma$  and  $b_r$  is defined as follows:

$$r^2(f) = \frac{|\Theta_{\Gamma b_r}(f)|^2}{\Theta_{\Gamma\Gamma}(f)\Theta_{b_r b_r}(f)}, \quad (5)$$

where  $\Theta_{\Gamma b_r}$  is cross-PSD,  $\Theta_{\Gamma\Gamma}$  and  $\Theta_{b_r b_r}$  are auto-PSDs, and  $f$  is cycle frequency (Carter et al., 1973). Generalizing signals to higher Cartesian dimensions is straightforward. The PSD in (5) can be estimated using the periodogram method (Bendat & Piersol, 2010).

Equation (2) suggests that the gravity gradient  $\Gamma_{zz}$  and topography are related through a radially symmetric operator. Hence, their 2-D periodograms are azimuthally averaged to obtain the *radially symmetric coherency*

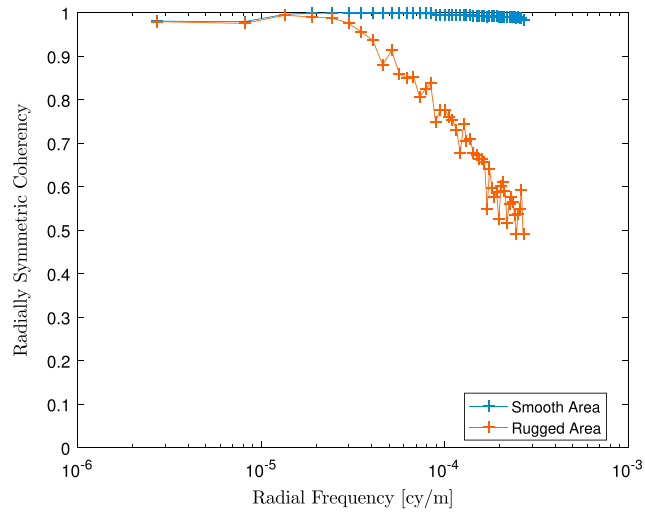


**Figure 3.** Radially symmetric coherencies between  $b_r$  and  $\Gamma_{zz}$  for the smooth and the rugged areas in Figure 2.

$\bar{r}^2(\bar{f})$ , which is a function of radial frequency (Marks & Smith, 2012). If the topography is given on a grid  $b_r(x, y) = b_r(l_x \Delta x, l_y \Delta y)$ ,  $l_x = 0, 1, \dots, N_x - 1$ ,  $l_y = 0, 1, \dots, N_y - 1$ , then its discrete Fourier transform is given by

$$\check{b}_{k_1, k_2} = \Delta x \Delta y \sum_{l_x = -\frac{N_x}{2}}^{\frac{N_x}{2}-1} \sum_{l_y = -\frac{N_y}{2}}^{\frac{N_y}{2}-1} b_{l_x, l_y} e^{-i2\pi \left( \frac{k_1 l_x}{N_x} + \frac{k_2 l_y}{N_y} \right)}, \quad (6)$$

where the indices  $k_1, k_2$  count off frequencies,  $f_{k_1} = \frac{k_1}{\Delta x N_x}$  and  $f_{k_2} = \frac{k_2}{\Delta y N_y}$ , respectively. If  $N_x$  is even,  $-\frac{N_x}{2} \leq k_1 \leq \frac{N_x}{2} - 1$ , and if  $N_x$  is odd,  $-\frac{N_x-1}{2} \leq k_1 \leq \frac{N_x-1}{2}$ , and similarly for  $f_{k_2}$ . The radially symmetric coherency is computed by

$$\bar{r}_k^2 = \frac{1}{M_k} \sum_{\bar{f}_{k-1} < \sqrt{f_{k_1}^2 + f_{k_2}^2} \leq \bar{f}_k} \frac{|\check{r}_{k_1, k_2}^* \check{b}_{k_1, k_2}|^2}{\check{r}_{k_1, k_2}^* \check{r}_{k_1, k_2} \check{b}_{k_1, k_2}^* \check{b}_{k_1, k_2}}, \quad (7)$$

where the asterisk denotes the complex conjugate,  $M_k$  is the number of discrete frequencies pairs  $f_{k_1}, f_{k_2}$  whose corresponding radial frequency lies in the interval  $(\bar{f}_{k-1}, \bar{f}_k]$ . Note that  $\bar{f}_k \leq \min(\frac{1}{2\Delta x}, \frac{1}{2\Delta y})$ .

The coherency is a frequency-domain analogue of the correlation coefficient. It indicates the linearity between the two data sets in the frequency domain regardless of their amplitude. Equation (2) suggests that under a first-term approximation the relationship between topography and gravity gradient can be described through a linear system. In the ideal case of a linear system without noise, the coherency should be 1 for all frequencies. In fact, (2) is only approximately true, so the coherency between  $\Gamma_{zz}$  and  $b_r$  deviates from one. Coherency close to one means that  $\Gamma_{zz}$  is attributed mostly to the linear part of the terrain effect. Coherency close to zero means that the gravity gradient  $\Gamma_{zz}$  and the topography  $b_r$  are independent.

In summary, at wavelengths where the coherency between the gravity gradient and the topography is large, we could use Parker's method to estimate the topography since the relation between  $\Gamma_{zz}$  and  $b_r$  is well represented by a linear system. At wavelengths where the coherency is small, we cannot estimate the topography from gravity gradients using a linear system due to significant nonlinear terms, as well as noise and/or other sources that falsify the relationship described in (2).

The radially symmetric coherency between topography and VGG for the smooth and the rugged areas, shown in Figure 2a, is computed using equation (7) and shown in Figure 3. The synthetic vertical gravity gradients (with no random error) are calculated through the theoretical equation (1) from topography data. In smooth area where topography and VGG are almost linearly related (see upper panel of Figure 2b), the coherency is large at all frequencies. In the rugged area where the nonlinearity is significant (see lower panel of Figure 2b), the coherency is large only at low frequencies. As frequency increases from  $2 \times 10^{-5}$  to  $2 \times 10^{-4}$  cy/m, the coherency quickly decreases from 0.95 to 0.5. At wavelengths shorter than 5 km, more than half of the VGG

is from the nonlinear terms of Parker's infinite series. In other words, if the topography is estimated through Parker's FFT-based method as described in section 2.1, the short wavelengths cannot be improved no matter how accurate the VGG measurements are.

### 2.3. Simulated Annealing Method

As shown in Figures 2b and 3, the nonlinear effect is nonnegligible in rugged areas like the one shown in Figure 6a. Simulated annealing (SA) is a candidate for a global optimization technique that can process nonlinear inverse problems. The vector containing the parameters to be determined is called the state of the system. The SA algorithm asymptotically finds an optimal state vector with probability 1, for which its cost function, a quality indicator that measures the discrepancy between the observations and the corresponding computed forward model, is at a global minimum (Kirkpatrick et al., 1983; Laarhoven & Aarts, 1987). In this subsection the SA method to estimate the seafloor topography is developed, for the purpose of improving the accuracy by employing a direct nonlinear model that relates topography and the gravity field.

#### 2.3.1. Introduction to the Simulated Annealing

The invention of SA is generally credited to Metropolis and his coworkers, who established an algorithm to simulate the process of annealing in thermal dynamics (Metropolis et al., 1953). Thirty years later, Kirkpatrick et al. (1983) found the connection between statistical mechanics and multivariate optimization and developed an algorithm called *simulated annealing* to minimize the cost function of a multivariate optimization problem by applying the Metropolis criterion. The simulated annealing algorithm was also independently developed by other scientists (Černý, 1985) during the same period. Since then, an increasing number of papers have been published for the refinement of the SA algorithm and its applications (Ingber, 1989; Laarhoven & Aarts, 1987; Szu & Hartley, 1987).

The SA algorithm starts with an arbitrary initial state  $\mathbf{b}_0$  whose cost function is  $E(\mathbf{b}_0)$ . Then a new state is generated with the probability  $a(\mathbf{b}_k)$  controlled by a parameter  $T_k$  called *temperature*, where  $k$  is the iteration step number. The new state is generated through  $b_k^i = b_{k-1}^i + y^i(B^i - A^i)$ ,  $i \in \{1, 2, \dots, D\}$  subject to  $A^i \leq b_k^i \leq B^i$ , where  $D$  is the number of elements in the state vector,  $y^i = \text{sgn}(u^i - \frac{1}{2})T_k^{|2u^i - 1|} - 1$ ,  $\text{sgn}()$  is the sign function,  $u^i$  is a random number generated from a uniform distribution in the interval  $[-1, 1]$ , and  $[A^i, B^i]$  is the allowed range of  $b^i$  (Ingber, 1989; Uzun, 2013). The next step is to compute the cost function of the new state,  $E(\mathbf{b}_k)$ , and then use the Metropolis criterion to determine whether to accept the new state or not. That is, if  $\Delta E = E(\mathbf{b}_k) - E(\mathbf{b}_{k-1}) \leq 0$ , the new state is accepted; and, if  $\Delta E > 0$ , the new state is accepted with the probability  $1 / [1 + \exp(\Delta E/T_k)]$ . Next, the temperature is decreased according to a cooling schedule, and a new state is generated to start another iteration cycle. This process is iterated until there is no change in the cost function.

It has been verified (Ingber, 1989; Laarhoven & Aarts, 1987) that if the cooling schedule is not faster than

$$T_k = T_0 \exp(-ck^{\frac{1}{D}}), \quad (8)$$

the probability distribution of the state  $a(\mathbf{b}_k)$  is given by the Boltzmann distribution

$$\lim_{T \rightarrow 0^+} \lim_{k \rightarrow \infty} a(\mathbf{b}_k) = \lim_{T \rightarrow 0^+} \lim_{k \rightarrow \infty} \Pr(\mathbf{b} = \mathbf{b}_k) = \frac{\exp\left\{-\frac{E(\mathbf{b}_k) - E_{\min}}{T_k}\right\}}{\sum_{\mathbf{b}} \exp\left\{-\frac{E(\mathbf{b}) - E_{\min}}{T_k}\right\}}. \quad (9)$$

In equation (8),  $c = me^{-\frac{n}{D}}$ , where  $m, n$  are free parameters to help tune the simulated annealing so that at the  $e^n$ -th iteration the temperature becomes  $T_0 \cdot e^{-m}$ . Note that the initial temperature  $T_0$  is set sufficiently high so that almost every state transition is accepted at the beginning. As the temperature decreases, the probability to reject the transitions that increases the cost function gradually approaches one. That is why the simulated annealing can jump out of a local minimum of the cost function at the beginning and ultimately land on the global minimum cost. As the temperature decreases, the Boltzmann distribution concentrates on the states with lowest cost, in other words, the state asymptotically converges to an optimal value with probability 1,

$$\lim_{T \rightarrow 0^+} \lim_{k \rightarrow \infty} \Pr(\mathbf{b}_k \in \mathbb{R}_{\text{optimal}}) = 1, \quad (10)$$

where  $\mathbb{R}_{\text{optimal}}$  is the set of global minimal states.



It can be seen from equation (8) that if the parameter dimension  $D$  is large, the increase of  $k^{\frac{1}{D}}$  becomes exponentially slow, which will slow the speed of temperature decrease and require prohibitively large computation resources. The simulated annealing turns to the next best choice by adding a quenching parameter  $Q$ :

$$T_k = T_0 \exp(-ck^{\frac{Q}{D}}), \quad (11)$$

where  $c = me^{-\frac{nQ}{D}}$ . The quenching parameter is of the same order as  $D$  and makes the simulated annealing lose its property of statistical convergence to the global minimum, although in practice it might still be among the best algorithms for a given system (Ingber & Rosen, 1992). Indeed, it has been successfully applied to a number of complex problems with large dimension (Raittinen & Kaski, 1990; Roy et al., 2005).

### 2.3.2. Forward Model and Cost Function

The seafloor depths (the parameters,  $\mathbf{b}$ ) in a forward model can be estimated through simulated annealing by minimizing a cost function, defined as the square of the  $L^2$  norm of the difference between the observed and forward-computed gravity gradients. Compared to the standard Parker's FFT-based method, SA only needs forward computation formulas and completely avoids linearization. SA also has no restrictions on data distribution, as required in Parker's infinite series model, thus enabling more flexibility, for example, when using airborne gravity gradient trajectories.

The practical implementation of the simulated annealing technique for seafloor depth estimation is described in the following. A local Cartesian coordinate system is set up with the origin located at the center of a study area and on the surface of the reference ellipsoid, and with  $x$ ,  $y$ , and  $z$  axes pointing to east, north, and up, respectively. Then the seafloor of the study area is modeled as a set of adjacent right rectangular prisms with edges parallel to the coordinate axes. The  $x$  and  $y$  coordinates of the right rectangular prisms are known. The  $z$  coordinate of the lower faces is the mean depth of the study area. The  $z$  coordinates of the upper faces represent the seafloor depths. They are the unknown parameters and are part of the state vector for simulated annealing.

The vertical gravity gradients at the sea surface, caused by the mass density of the seafloor topography, are computed using the aforementioned right rectangular prism model (Blakely, 1996; Zhu, 2007). Given the mean sea depth, the topography can always be related to the depth through  $b_i = b - d$ . Only the *near zone* effect is considered, as defined in section 2.3.3. That is, for each computation point, only the prisms within a preset distance are included. The VGG is computed at the evaluation point at sea level due to each prism and then summed. The *far zone* effect  $\Delta\Gamma_{zz}^{\text{far}}$  is of long-wavelength type and approximated by a constant for the entire study area (the validity of this assumption is discussed in section 2.3.3). This parameter (far zone effect) is unknown and added to the state vector  $\mathbf{b}$  to be determined. A schematic diagram is shown in Figure 4. The density difference between the sea water and seabed is assumed to be constant. In summary, the state vector to be determined contains the seafloor depths and the gravity gradient offset due to mass outside the near zone. The VGG at each computation point is the sum of vertical gravitation gradients caused by the near zone prisms and the offset due to the far zone mass, with the density of the prism assumed constant,

$$i\Gamma_{zz}^{\text{comp}}(\mathbf{b}) = \Delta\Gamma_{zz}^{\text{far}} + \sum_{j=1}^M i\Gamma_{zz}^{\text{comp}}(b_j), \quad (12)$$

where  $i\Gamma_{zz}^{\text{comp}}(\mathbf{b})$  is the computed VGG at  $i$ ,  $\mathbf{b} = \{b_1, b_2, \dots, b_M, \Delta\Gamma_{zz}^{\text{far}}\}$  is the state vector,  $M$  is the number of right rectangular prisms within the near zone, and  $i\Gamma_{zz}^{\text{comp}}(b_j)$  is the VGG at  $i$  due to a right rectangular prism  $j$  and is computed using

$$i\Gamma_{zz}^{\text{comp}}(b_j) = G\Delta\rho \cdot \arctan \frac{(x - \xi)(y - \eta)}{(z - \zeta)\sqrt{(x - \xi)^2 + (y - \eta)^2 + (z - \zeta)^2}} \Big|_{\xi=xw_j}^{x=x_e} \Big|_{\eta=ys_j}^{y=y_e} \Big|_{\zeta=md_j}^{b_j}, \quad (13)$$

where  $G$  is Newton's gravitational constant,  $\Delta\rho$  is the density difference between sea water and seafloor topography,  $(x, y, z)$  are the coordinates of the location of observation point  $i$ ,  $(\xi, \eta, \zeta)$  are the variables of integration over the right rectangular prism,  $xw_j, x_e, ys_j, y_e$  are the  $x$  axis and  $y$  axis boundaries for the  $j$ th prism,  $md_j$  is the  $z$  coordinate of mean depth at  $j$ , and  $b_j$  is the  $z$  coordinate of seafloor at  $j$  (Zhu, 2007).

The search limit of the unknown seafloor depth,  $[A^i, B^i]$ , can be set to constant values, for example, the upper search limit could be set to the sea surface and the lower limit could be set to 1 km below the maximum depth

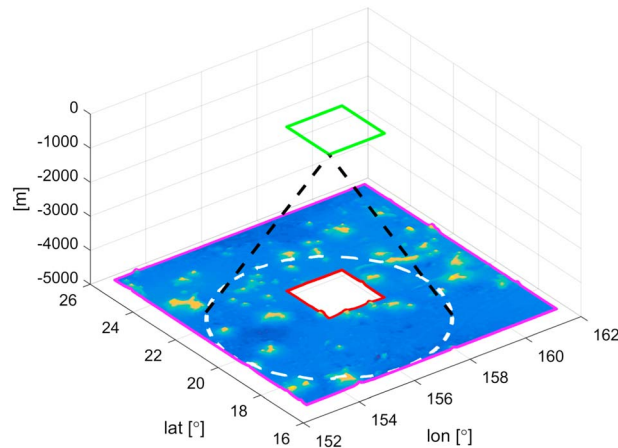


**Figure 4.** The green rectangle represents the range of observed vertical gravity gradients. The area directly beneath it and marked by a red rectangle is the unknown seafloor depth to be estimated. The depth between the red and the magenta rectangles is fixed values from SIO global topography model version 18.1. It is called the padding area. In this figure, the dashed white circle marks the near zone depth needed to forward compute the vertical gravity gradient at the west-south corner. The radius of the dashed white circle is the truncation distance  $s_0$  that defines the near zone.

over the study area. But the computations are inefficient if one uses too large a search space. Considering the facts that the SIO global topography model is based on a fit to ship soundings (Smith & Sandwell, 1997) and that our SA method mainly improves the estimation of the topography due to originally neglected nonlinear effects which are not large, the search space was reduced by setting the upper and lower search limits of the seafloor depth at each grid point to 1 km above and 1 km below the depth value interpolated from the SIO global topography model. The mean of the difference between the VGG observations and the VGG forward computed from the SIO global topography model indicates the magnitude of the offset due to far zone mass and thus is considered when setting the search limit of  $\Delta\Gamma_{zz}^{\text{far}}$ . For example, in the study area described in section 3.1, the mean of the difference is  $-3$  Eötvös. Then the search domain for the gravity gradient offset due to far zone mass is empirically set to  $-6 \text{ Eötvös} \leq \Delta\Gamma_{zz}^{\text{far}} \leq 0 \text{ Eötvös}$ .

The data used to estimate the depth are vertical gravity gradients derived from satellite altimetry using derivatives of the vertical deflections. These data are called the *observed* gravity gradients (Rummel & Haagmans, 1990; Sandwell & Smith, 1997). There are differences between the computed and observed vertical gravity gradients. The objective is to find the optimal state vector by using the SA that minimizes these differences. The cost function is defined as the average of squared differences between the computed and the observed vertical gravity gradients,

$$E(\mathbf{b}) = \frac{1}{N} \sum_{i=1}^N \left[ i\Gamma_{zz}^{\text{obs}} - i\Gamma_{zz}^{\text{comp}}(\mathbf{b}) \right]^2, \quad (14)$$

where  $N$  is the number of observation points,  $i\Gamma_{zz}^{\text{obs}}$  is the vertical-VGG observed at  $i$ .

### 2.3.3. Truncation and Resolution Errors in the Forward Computation

In practice, the gravity gradient is forward computed from a discrete digital topography model within a preset near zone. For each computation point, its *near zone* is defined as the area in which the horizontal distance between a prism and the computation point is within a preset truncation distance  $s_0$ . Area outside the near zone is defined as *far zone*. The *truncation error* is defined as the error at one point caused by neglecting the far zone effect in the forward computation. In this analysis, the truncation error was assumed to be of long-wavelength character and was approximated by a constant. In order to validate this assumption, one can compute the *relative truncation error*, which is the difference between truncation errors of two points both in the study area but separated by a horizontal distance  $l$ . If the relative truncation error is smaller than the level of observation noise, then we could use just one parameter to represent the truncation errors in the entire area; see equation (12). If the relative truncation error is large, then our assumption that the truncation error is a constant is not tenable. In addition, the forward computation uses discrete topography with finite



resolution and thus causes an error called the *resolution error*. The equation to estimate the variance of the relative truncation error is given by (refer to Jekeli, 2013; Yang, 2017, for details)

$$\left(\sigma_{\Delta\epsilon_{zz}^{\text{trunc}}}\right)^2 = 4\pi(G\Delta\rho)^2 \int_{\bar{f}=0}^{\infty} \left|\ddot{\omega}_{zz}(\bar{f})\right|^2 \bar{\Theta}_{b_r,b_r}(\bar{f}) \left[1 - J_0(2\pi\bar{f}l)\right] \bar{f}d\bar{f}, \quad (15)$$

where  $\bar{\Theta}_{b_r,b_r}(\bar{f})$  is the azimuthally averaged periodogram of the topography  $b_r$ ,  $J_0$  is the zero-order Bessel function of the first kind, and  $\ddot{\omega}_{zz}(\bar{f})$  is given by

$$\ddot{\omega}_{zz}(\bar{f}) = (2\pi)^2 \bar{f} e^{2\pi\bar{f}d} + 2\pi \int_{s'=0}^{s_0} \left[ \frac{1}{(s'^2 + d^2)^{\frac{3}{2}}} - \frac{3d^2}{(s'^2 + d^2)^{\frac{5}{2}}} \right] J_0(2\pi\bar{f}s') s' ds', \quad (16)$$

where  $s' = \sqrt{x^2 + y^2}$ .

If the PSD of the topography is approximated by a power law,  $\bar{\Theta}_{b_r,b_r}(\bar{f}) = C\bar{f}^{-\beta}$ , the variance of the resolution error is estimated by (Jekeli, 2013; Yang, 2017)

$$\left(\sigma_{\epsilon_{zz}^{\text{res}}}\right)^2 = 2^{2\beta-3} \pi^{\beta+1} (G\Delta\rho)^2 C d^{\beta-4} \Gamma^{\text{uigf}}(4-\beta, 4\pi d\bar{f}_N), \quad (17)$$

where  $\Gamma^{\text{uigf}}(p, z)$  represents the upper incomplete gamma function, and  $\bar{f}_N = \sqrt{\frac{1}{(2\Delta x)^2} + \frac{1}{(2\Delta y)^2}}$ .

### 3. Numerical Experiment

#### 3.1. Study Area and Data Sets

The simulated annealing technique developed in the last section for seafloor depth estimation is tested using data in a  $2^\circ \times 2^\circ$  area located in the West Pacific Ocean and bounded by latitudes  $20^\circ$  and  $22^\circ$  north, and longitudes  $156^\circ$  and  $158^\circ$  east.

The  $1' \times 1'$  VGG model version 24.1 is downloaded from the website of the SIO (Sandwell et al., 2014); see Figure 5a. The VGG is calculated using the derivatives of the vertical deflections (Sandwell & Smith, 1997, Appendix B). In Sandwell and Smith (1997), it is reported that all the along-track data were filtered with the same filter to ensure a common bandwidth (0.5 gain at 18-km wavelength). No such description is found in Sandwell et al. (2014), which updates the SIO gravity model using the Cryosat-2 and Jason-1 data. The two missions have nominal track spacing of 2.5 and 7.5 km, respectively. The accuracy of the altimetry-derived gravity anomaly released by SIO is  $\pm 2$  mGal (Sandwell et al., 2014). The accuracy of the VGG derived from the same altimetry data sets is not reported. A rough analysis by applying the law of error propagation to equation (A6) in Sandwell and Smith (1997), with the derivatives of the vertical deflections substituted by a numerical differentiation formula, shows that the accuracy of VGG released by SIO is about  $\pm 4$  Eötvös. This assumed that accuracy is adequate for present purposes in the absence of a more detailed analysis.

The ship sounding depths are downloaded from the National Centers for Environment Information ([www.ngdc.noaa.gov/maps/bathymetry](http://www.ngdc.noaa.gov/maps/bathymetry)) and shown in Figure 6a. The spatial resolution in 2-D is not uniform due to nonuniform ship tracks. No accuracy information comes with these depths. The ship sounding depths are treated as true values; an analysis of 2,253 cruise surveys shows that the median absolute value of the crossover errors at intersecting ship tracks is 26 m (Smith, 1993), which is much smaller than the accuracy of gravity predicted seafloor topography. This study also uses the global topography model version 18.1 released by the SIO (Smith & Sandwell, 1997).

#### 3.2. Estimation Using Simulated Annealing

##### 3.2.1. Determination of Truncation Distance

Based on the power law model which best fits the log-log plot of the PSD of the topography shown in Figure 6b in a least squares sense,  $\bar{\Theta}_{b_r,b_r}(\bar{f}) = 0.0043 \times \bar{f}^{-3.4319}$ , the standard deviation of the relative truncation error as a function of the truncation distance  $s_0$  from the computation points was calculated through equation (15) and is shown in Figure 7.

Figure 7 shows that, for a given  $l$ , increasing the truncation distance,  $s_0$ , reduces the relative truncation error. Figure 7 also shows that for a given  $s_0$ , the relative truncation error increases as the separation distance  $l$

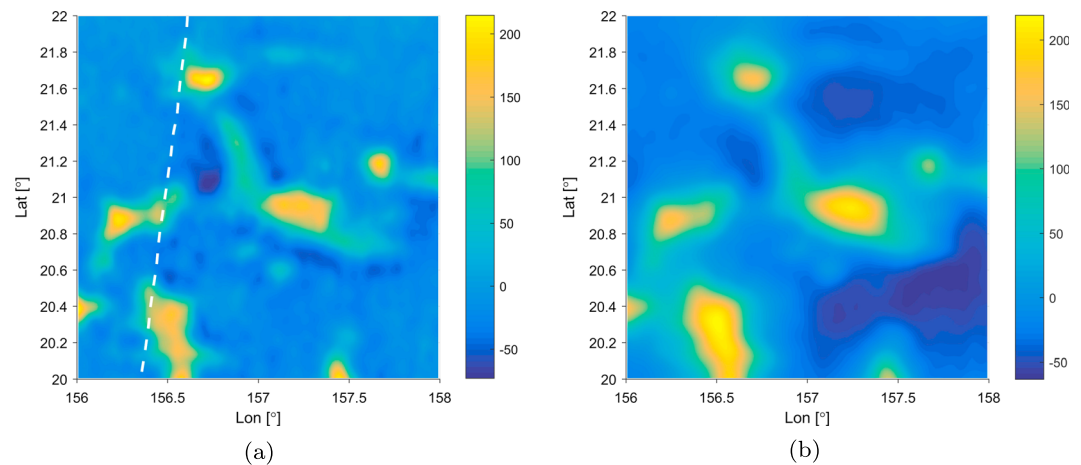


**Figure 5.** (a) The  $1' \times 1'$  vertical gravity gradients of the study area. The units of the color bar are Eötvös. The dashed white line is the ship track of the vessel *JOIDES Resolution*. It is not used in the experiment and is reserved for the accuracy test. (b) The  $1' \times 1'$  gravity anomalies of the study area. The units of the color bar are mGal.

increases. This suggests that a small study area should be adopted for simulated annealing, considering that as implemented here the far zone effect is assumed to be a constant. If the study area is large, then we should divide it into several small regions and invert one region at a time; otherwise, the assumption of a constant far zone topography effect is no longer valid. A small study area also leads to a smaller number of seafloor depth parameters and thus benefits the simulated annealing by allowing a faster temperature cooling schedule.

On the other hand, because the topography to be determined is surrounded by a padded-topography model, errors in this background model propagate to the estimated topography. This propagated error is larger at the edge of the study area where more of the padded-topography model is used. To reduce this error, the topography to be estimated by SA should cover as large an area as possible.

Combining the two considerations above, given the size of the study area represented by  $l$ , the truncation distance  $s_0$  can be set to the smallest value whose corresponding relative truncation error is small enough, so that the far zone effect can be assumed uniform for the entire study area. The study area for one inversion remains at  $2^\circ \times 2^\circ$  (about  $222 \text{ km} \times 222 \text{ km}$ , that is,  $l = 222 \text{ km}$ ), so the truncation distance is set to 350 km. Figure 7 shows that the relative truncation error is reduced to 3 Eötvös, which is smaller than the assumed VGG data accuracy.

Because the data do not contain information higher than the Nyquist frequency, the sampling intervals of the VGG and the seafloor topography limit the resolution that the SA method can achieve. The grid size of the VGG

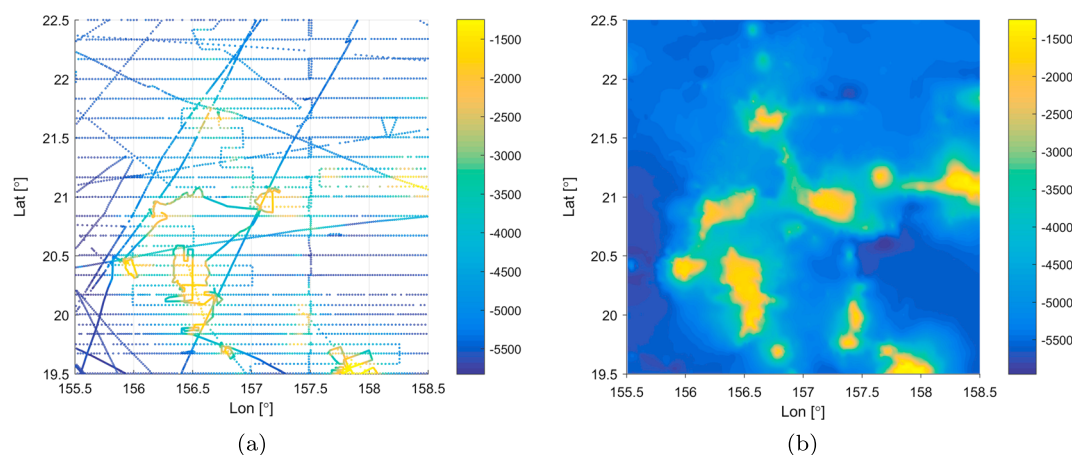


**Figure 6.** (a) Single-beam ship sounding data downloaded from National Centers for Environment Information's website. (b) The seafloor depths interpolated from Figure 6a through biharmonic spline interpolation. The units are meters.

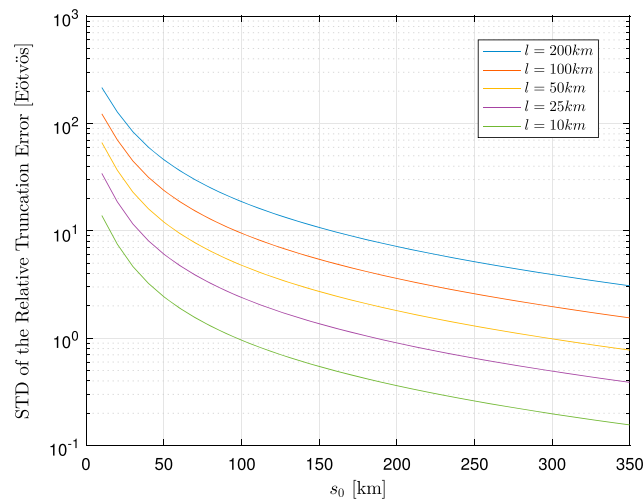


**Figure 7.** Relative truncation error between two points separated by a horizontal distance  $l$  versus truncation distance  $s_0$ . The mean sea depth is  $d = -4828.8$  m in the study area.

data is  $1' \times 1'$ , corresponding to a Nyquist wavelength of about 3.7 km. Therefore, there is no need to use intervals shorter than 1.85 km when building topography models. The resolution error computed through equation (17) is  $8.8 \times 10^{-7}$  Eötvös, which is negligible.

### 3.2.2. Results and Evaluation

The seafloor depth is estimated from VGG shown in Figure 5a using the simulated annealing method described in section 2.3 and with tuning parameters listed in Table 1.

In this experiment, the SA iteration is terminated when the number of iterations reaches  $1 \times 10^6$ . There are typically other criteria (e.g., terminate the iteration when the difference in cost function between transitions is smaller than a preset threshold for a certain number of times), but this has proved to be adequate (Yang, 2017) and provides accurate control of the program running time. Figure 8a indicates that the cost decreases as the iteration number increases. It has dropped less than 2 orders of magnitude during the annealing process. The number of the iterations needed by the SA to converge is related to the number of unknown parameters in the state. The greater the number of unknown parameters, the more iterations are needed.

A new state is generated by adding a disturbance to the old state. The disturbance is a stochastic variable controlled by the temperature. Figure 8b indicates that at the beginning when the temperature is high, the disturbance and the resulting  $|\Delta \text{cost}|$  are large. Most of the new states are accepted even if they increase the cost function. As the iteration proceeds, the temperature decreases exponentially. This leads to a gradually diminishing disturbance and  $|\Delta \text{cost}|$ . That is, the probability distribution of the disturbance gradually concentrates on a smaller disturbance. As the temperature decreases, the probability of accepting the transitions which increase the cost function gradually becomes low. The Metropolis criterion ensures that the transition which increases the cost function can be accepted with probability  $>0$ ; thus, the states have the ability to escape from a local minimum. At the end stage when the temperature is low, this probability becomes low as well, so that only the transitions reducing the cost function are accepted. In the meantime, the state and the  $|\Delta \text{cost}|$  can only change by a small amplitude. The state is then refined only marginally and the cost function approaches the global minimum.

An initial estimation of the seafloor depth as obtained through simulated annealing is shown in Figure 9a, and its PSD is shown in Figure 9b. The other parameter in the state vector, the gravity gradient offset due to mass outside the near zone, is  $-3.1$  Eötvös. The PSD of the depth may be approximately represented

**Table 1**  
The Tuning Parameters

$T_0$	$n$	$m$	$D$	$Q$
1	$\log(1e7)$	$-\log(1e-4500)$	16,506	16,506

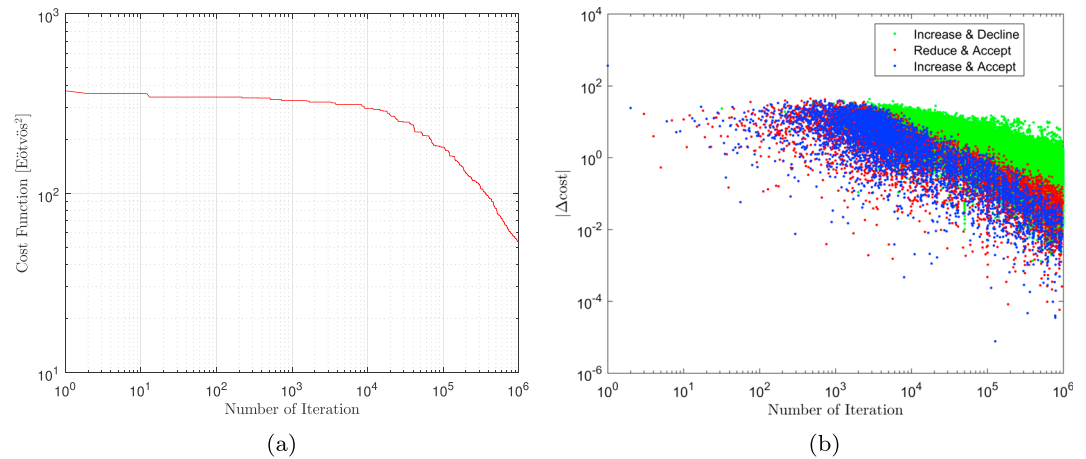


**Figure 8.** (a) The cost function decreases during annealing. (b) The change of cost function between transition. Red dots mean that the newly generated state reduces the cost function, and the transition to the new state is accepted. Green dots mean that the new state increases the cost function, and the transition to the new state is rejected by the Metropolis criterion. Blue dots mean that the newly generated state increases the cost function, but the transition is accepted.

by a power law (Jekeli, 2013), namely, a straight line with negative slope in the log-log figure. Therefore, in Figure 9b the power at frequencies higher than  $7 \times 10^{-5}$  cy/m (approximately 14-km wavelength) represents mainly errors in the estimation. One may claim that the seafloor depth was recovered from the vertical gravity gradient, but the result contains high-frequency errors. The next step is to design a low-pass filter for the result and analyze the estimation accuracy.

The high-frequency error is generated due to the large dimensionality of the inversion and the comparatively small number of iterations used. Several simple numerical tests using errorless, simulated topography and VGG data sets show that as the number of unknown topography parameters increases, the estimation accuracy of SA decreases and the error is of high-frequency character. As the number of topography parameters increases, the cooling schedule (8) becomes prohibitively slow and thus the needed computation load increases exponentially fast. As a compromise, (11) is used instead. This leads to a smaller number of iterations, but the cooling schedule decreases faster.

The Gaussian low-pass filter with cutoff wavelength of 15 km,

$$W_{15} = e^{-2 \times (2.8109 \times 10^3 \pi \bar{f})^2}, \quad (18)$$

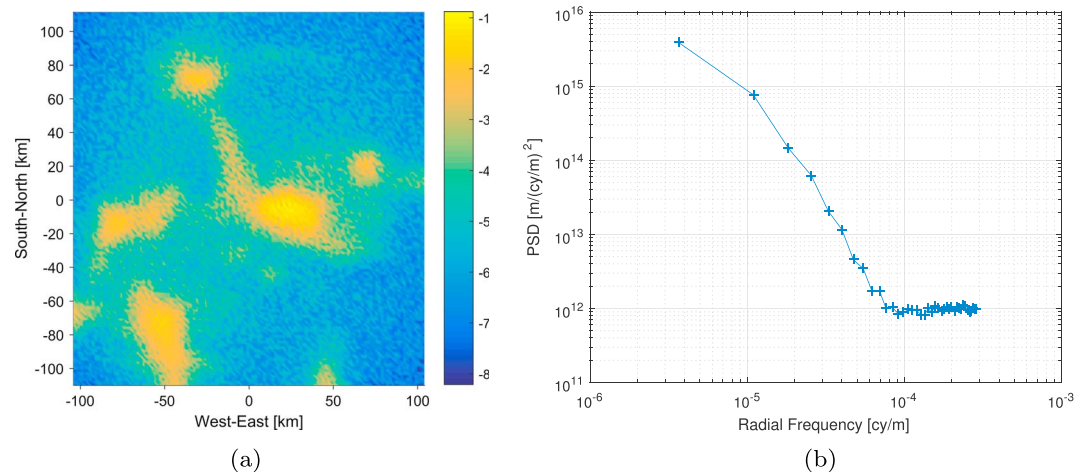


**Figure 9.** (a) The seafloor depth estimated through simulated annealing. The units of the color bar are kilometers. (b) The Power spectral density of the depth estimation. PSD = Power-Spectral-Density.

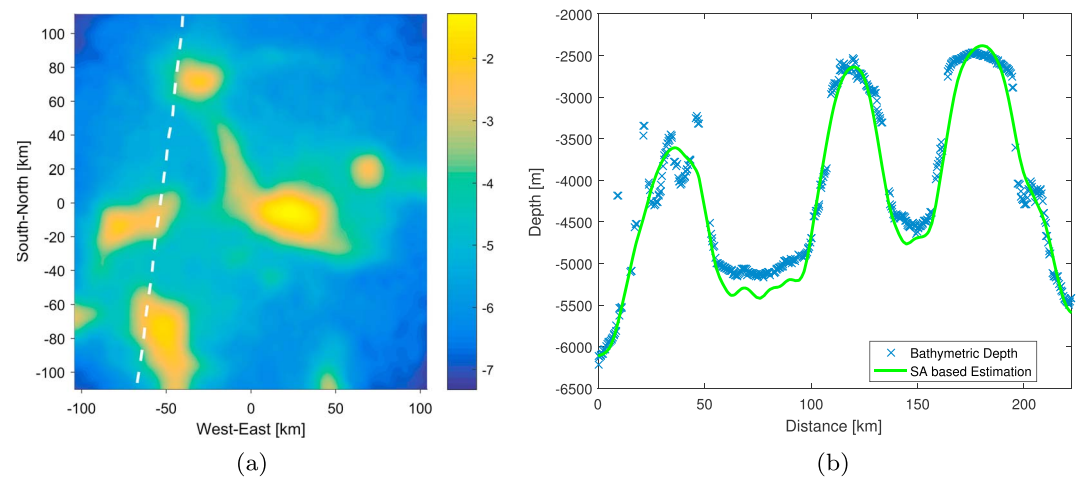


**Figure 10.** (a) The filtered depth estimation. The units of the color bar are kilometers. (b) The blue crosses are bathymetric depths measured by the vessel *JOIDES Resolution*. The green solid line is the depth at corresponding locations estimated through simulated annealing. The distance axis corresponds to the slice going from north to south. SA = simulated annealing.

is applied to the seafloor depth estimation shown in Figure 9a. It is the same filter as in Smith and Sandwell (1994) in order to make their topography model comparable with the SA results. The filtered estimates are shown in Figure 10.

At the mesh nodes constrained by ship sounding, the difference between the depth estimated by the SA method and the ship bathymetric depth was computed. The statistics of the differences are shown in Table 2.

The histogram of these differences is shown in Figure 11a. The skewness of these differences is 0.88. Because the peak of the histogram is sharp, and the tails are longer than those of the normal distribution, the root-mean-square (RMS) cannot fully represent the distribution. Smith and Sandwell (1994) and Calder (2006) also observe similar long-tailed RMS distributions. So the cumulative distribution of the absolute difference is also computed and presented in Figure 11b. It shows that half of the absolute differences are smaller than 112 m. More than 75% of the differences are smaller than 200 m.

### 3.2.3. Other Tests of the Simulated Annealing Algorithm

As shown in Figure 1, the VGG is not sensitive to the long-wavelength topography due to the factor  $-2\pi\bar{f}$  in the gradient admittance. Therefore, removing the long wavelengths from the VGG and the topography may improve the estimation accuracy.

This idea was tested by applying the low-pass filter

$$W_l = e^{-2 \times (2.9983 \times 10^4 \pi \bar{f})^2} \quad (19)$$

to the ship sounding data shown in Figure 6b to obtain wavelengths longer than 160 km. The long-wavelength depth, rather than the mean depth, is then used as the bottom boundary of the prisms that represent the seafloor, and the seafloor depth still served as the upper boundary of the prism. The forward-modeled VGG is thus attributed strictly to the shorter wavelengths of the seafloor depth and computed by

$$i\Gamma_{zz}^{\text{comp}}(b_j) = G\Delta\rho \cdot \arctan \frac{(x - \xi)(y - \eta)}{(z - \zeta)\sqrt{(x - \xi)^2 + (y - \eta)^2 + (z - \zeta)^2}} \Big|_{\xi=x_{W_j}}^{x_{E_j}} \Big|_{\eta=y_{S_j}}^{y_{N_j}} \Big|_{\zeta=z_{T_j}}^{b_j}, \quad (20)$$

**Table 2**

*The Statistics of the Difference Between Depth Estimation and the Ship Soundings at Constrained Mesh Nodes*

Max absolute	Mean	STD	RMS	95th Percentile
1307.69	2.37	235.95	235.97	395.61

*Note.* The units are meters. STD=standard deviation; RMS = root-mean-square.

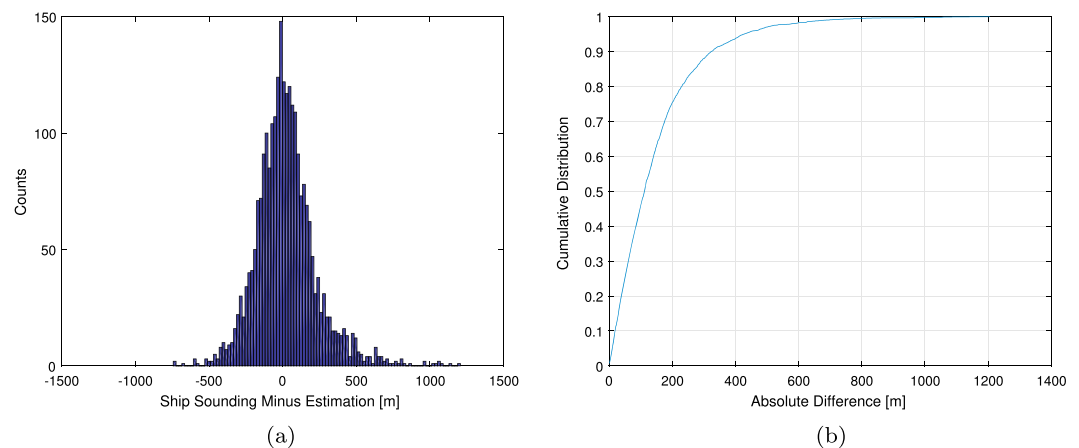


**Figure 11.** (a) The histogram of the difference between ship soundings and estimation. (b) The cumulative distribution of the absolute difference between ship sounding and estimation.

where  $l_{rt_j}$  is the  $z$  coordinate of the long-wavelength regional depth at  $j$ , and all other notations have the same meaning as in (13).

The high-pass filter  $W_h = 1 - W_l$  is applied to the observed VGG shown in Figure 5a to obtain wavelengths shorter than 160 km. The difference between the forward computed and *observed* 0- to 160-km wavelength VGG is used in the computation of the cost function.

Besides removing long wavelengths, another test is also conducted to see the effects of using a smaller truncation distance.

In test 0, the truncation distance is 49 km, and the study area spans  $2^\circ$  (about 220 km) along latitude and longitude. Figure 7 shows that the corresponding maximum relative truncation error is about 50 Eötvös, which is not acceptable and suggests adopting a larger truncation distance. The test 0 served as a reference. Tests 1 to 2 modify one condition at a time. Compared with test 0, test 1 increases the truncation distance to 350 km (this is the numerical experiment shown in section 3.2.2). Then based on test 1, test 2 removes the long wavelengths from the observed vertical gravity gradient, and forward computes the VGG using masses between seafloor depth and long-wavelength depth.

The statistics of the results are shown in Table 3, which indicates that increasing the truncation distance significantly improves the estimation accuracy. This modification reduces the maximum absolute value of the difference between the estimated seafloor depths and the ship sounding measurements, as well as the STD and RMS value of this difference. However, the improvements obtained by removing the long wavelengths are not significant, since the VGG caused by the long-wavelength depth is small.

### 3.3. Comparison of the Estimation Results

The global topography model (Smith & Sandwell, 1994, 1997), released by SIO, has been incorporated into most publicly available global seafloor topography models, like Google Earth and the General Bathymetric Chart of the Oceans (Marks & Smith, 2006; Marks et al., 2010). It was predicted from altimetry-derived gravity anomalies using Parker's formulation. In this subsection, it is used to compare with the estimation result

**Table 3**

*The Statistics of the Differences Between Depth Estimation by Simulated Annealing and the Ship Soundings at Constrained Mesh Nodes*

Test no.	Settings		Results (m)				
	$s_0$ (km)	$W_l$ applied	Max absolute	Mean	STD	RMS	95th Percentile
0	49	✗	1,379.66	−4.68	308.80	308.89	496.25
1	350	✗	1,307.69	2.37	235.95	235.97	395.61
2	350	✓	1,206.30	−11.31	224.74	225.02	352.19

Note. The units are meters. STD=standard deviation; RMS = root-mean-square.



**Table 4***The Statistics of the Differences Between Smith and Sandwell's Unadjusted Prediction and the Ship Sounding at Constrained Grid Cells*

Max absolute	Mean	STD	RMS	95th Percentile
1,761.39	2.77	301.26	301.28	438.80

Note. The units are meters. STD=standard deviation; RMS = root-mean-square.

in section 3.2, namely, the seafloor depth estimated from altimetry-derived gravity gradients using simulated annealing. Note that Smith and Sandwell (1997) modified their topography prediction to force the predicted topography at grid cells constrained by ship soundings to fit the bathymetry-implied heights. Therefore, their unadjusted prediction, rather than the final released version of the global topography, is used in the present comparison. The difference between their unadjusted topography prediction and the constraining ship soundings was calculated. The statistics of the difference are shown in Table 4.

All conditions for the two estimation methods such as gridding interval, filters, cutoff frequency are set to be as close as possible. Both estimations assume that the density of the topography is uniform and make use of a relationship between topography and gravity gradients, although one is in the frequency domain and the other in the space domain. The estimations with the SA method are performed in the same spectral band of wavelengths as the SIO global topography model, namely, for wavelengths longer than 15 km. Although the Nyquist wavelength of the topography and VGG data sets in the two methods is about 3.5 km, the same Gaussian low-pass filter with cutoff wavelength of 15 km is applied to both depth estimations.

Comparison between Tables 4 and 2 shows that under certain limitations (applying filters, assuming constant density, and errorless ship sounding), the RMS of the differences with respect to the ship soundings for the gradient estimated topography by simulated annealing is about 22% smaller than the gravity anomaly predicted topography by Parker's formulation. Since the estimations in both methods perform in the same spectral band of wavelengths, this improvement is mainly attributed to the removal of the linear approximation in the modeled relationship between gravity gradient and topography.

The profile along the ship track of *JOIDES Resolution* is shown in Figure 12a, which shows that, except in a flat region (i.e., for a distance between 55 and 95 km), the SA estimation is generally closer to the bathymetric depths than SIO's FFT-based estimation. The misfit between SA estimated topography and ship soundings in the flat region might be caused by thick sediments over variable density ocean bedrock. In the distance between 55 and 95 km, the gravity gradient has a large signal but the topography is smooth. In this kind of region, where gravity anomaly does not correlate with seafloor topography, Smith and Sandwell's (1994) seafloor estimate only depends on long-wavelength ship soundings, so their seafloor estimate is closer to the bathymetric depths.

Hu et al. (2014) tested their method in the same area. However, they interpolated the topography-to-gradient admittance at control points onto the whole topography grid, which makes their prediction method to some extent similar to direct interpolation of ship soundings. Besides, they compared the ship soundings with the polished SIO model (final released version, which itself should fit the ship soundings) rather than the unpolished one. As a result, the RMS of their computed difference is only 69.52 m.

#### 4. Summary and Conclusions

Compared with the gravity anomaly, the gravity gradient is more sensitive to the short-wavelength topography. This research attempted to improve the current standard seafloor topography estimation methods by removing the linear approximation in the modeled relationship between gravity and topography.

Numerical analysis shows that in rugged areas (topography ranges from  $-1$  to  $-5$  km over a 200 km by 200 km rectangular area), the nonlinear terms of Parker's series are not negligible. This is supported by an algorithmic analysis of simulated topography using the radially symmetric coherency, which is a frequency-domain analogue of the correlation coefficient, and indicates how much of the observed gravity gradient is attributed to the linear part of the terrain effect. In the synthesized rugged area, the analysis shows that at short wavelengths, more than half of the implied VGG is from the nonlinear terrain effect if the density of the topography

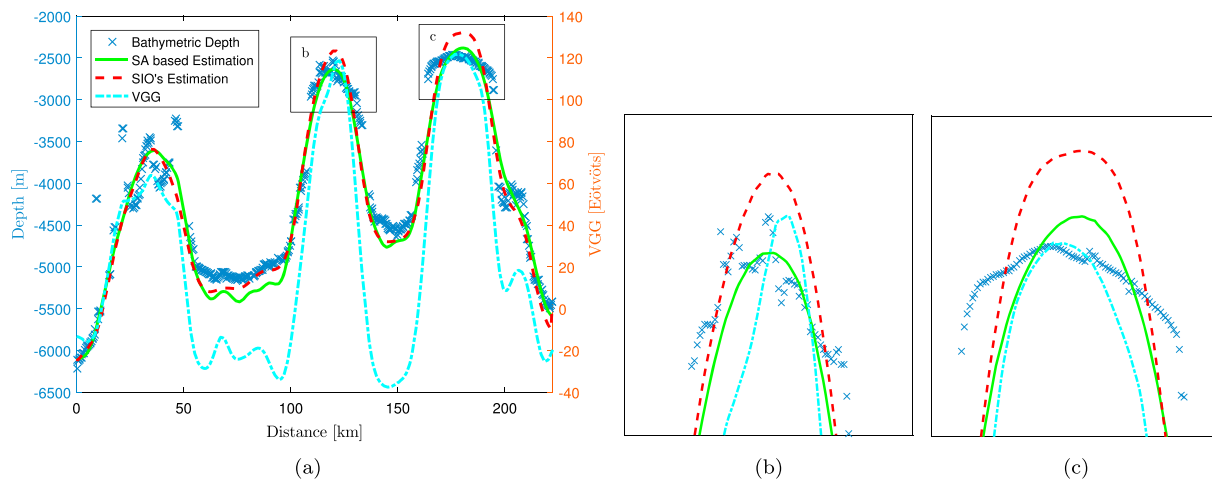


**Figure 12.** (a; left y axis) The blue crosses are bathymetric depths measured by the vessel *JOIDES Resolution*. The green solid line is the depth along the ship track estimated in section 3.2. The red dashed line is the depth model released by Scripps Institution of Oceanography (SIO). (right y axis) The cyan dot dashed line is from the vertical gravity gradients along the ship track. (b) and (c) zoom in on the boxed regions shown in Figure 12a, respectively. SA = simulated annealing; VGG = vertical gravity gradient.

is assumed constant. This finding means that in rugged areas, the accuracy of the Fourier transform based method quickly decreases as the frequency increases, no matter how accurate the gravity gradient measurement is and how high the resolution is. For gravity and gravity gradient measurements, usually, it is not easy to significantly improve the measurement accuracy. Therefore, it is important to study how to make use of the nonlinear terms before we seek more precise gravity gradient measurements to improve the estimation accuracy.

To employ nonlinear terms in the estimation of seafloor topography from gravity gradients, a global optimization technique called simulated annealing is used, which can process nonlinear inverse problems. This method is tested in a  $2^\circ \times 2^\circ$  area in the West Pacific Ocean using altimetry-derived gravity gradients. The seafloor depth parameters are estimated through SA by minimizing the difference between the observed and forward-computed vertical gravity gradients. Two processing steps are critical to achieve success. Padding (i.e., extending) the vicinity of the study area with a known topography model and including sufficient extent of topography are needed for the upward continuation in the forward model to ensure that the relative truncation error is below the level of observation noise, and thus enabling the modeling of the far zone effect as a constant.

The estimated depths were compared with single-beam bathymetric depths downloaded from National Centers for Environment Information. The RMS of the difference between them for the simulated annealing method is  $\pm 236$  m, which is 22% smaller than that of the SIO's global topography model over the study area.

Although there is a tremendous computational burden with SA, this cost in the coming *big data* and *artificial intelligence* era is decreasing fast. It is worthwhile to trade computation costs for better accuracy and resolution in the estimation of seafloor topography. Another advantage of the simulated annealing technique is that it has no restrictions on data distribution, as required in Parker's infinite series model, thus enabling the use of data from an airborne gravity gradiometer, whose resolution is high but flight trajectory may be irregular.

The simulated annealing method developed in this research may be useful in updating the global seafloor topography, especially in rugged areas. But this method and the Fourier transform method are limited to areas where subtopography density can be assumed uniform. The existence of places where subsurface geologic structures are complex and are the main source for gravity gradients impedes topography estimation from gravity gradients. Identifying this kind of area is an interesting topic for future research. Further investigations need to be performed to optimally combine different gravity gradient tensor elements or combine gravity gradient and gravity anomaly from independent sources. The purpose of the former is to increase the signal-to-noise ratio, and the objective of the latter is to combine the superiorities of the gravity gradient and the gravity anomaly at different frequencies.

## Acknowledgments

The authors are thankful to David T. Sandwell for providing the unadjusted seafloor topography prediction. This research is supported in part by the Friend of Orton Hall travel award. Computations were partially supported by the Ohio Supercomputer Center ([www.osc.edu/resources/getting\\_started/citation](http://www.osc.edu/resources/getting_started/citation)). Some of the work was done while Junjun Yang was studying in the Geodetic Science Ph.D. program, The Ohio State University, and while he was working in the Institute of Geodesy and Geophysics, Chinese Academy of Sciences. The vertical gravity gradient data and the SIO global topography models used in this paper are available at <ftp://topex.ucsd.edu/pub/>. The ship sounding depths can be downloaded from [www.ngdc.noaa.gov/maps/bathymetry](http://www.ngdc.noaa.gov/maps/bathymetry). Comments from two anonymous reviewers were highly appreciated as they led to a significant improvement of the original manuscript.

## References

- Barnes, G. J., Lumley, J. M., Houghton, P. I., & Gleave, R. J. (2011). Comparing gravity and gravity gradient surveys. *Geophysical Prospecting*, 59, 176–187. <https://doi.org/10.1111/j.1365-2478.2010.00900.x>
- Bendat, J. S., & Piersol, A. G. (2010). *Random data: Analysis and measurement procedures*, Wiley Series in Probability and Statistics (4th ed.). Hoboken, NJ: John Wiley & Sons.
- Blakely, R. J. (1996). *Potential theory in gravity and magnetic applications* (pp. 184–195). Cambridge, UK: Cambridge University Press. <https://doi.org/10.1017/CBO9780511549816>
- Calder, B. (2006). On the uncertainty of archive hydrographic data sets. *IEEE Journal of Oceanic Engineering*, 31, 249–265. <https://doi.org/10.1109/JOE.2006.872215>
- Carter, G. C., Knapp, C., & Nuttall, A. H. (1973). Estimation of the magnitude-squared coherence function via overlapped fast Fourier transform processing. *IEEE Transactions on Audio and Electroacoustics*, 21(4), 337–344. <https://doi.org/10.1109/TAU.1973.1162496>
- Černý, V. (1985). Thermodynamical approach to the traveling salesman problem: An efficient simulation algorithm. *Journal of Optimization Theory and Applications*, 45(1), 41–51. <https://doi.org/10.1007/bf00940812>
- Dixon, T. H., Naraghi, M., McNutt, M. K., & Smith, S. M. (1983). Bathymetric prediction from Seasat altimeter data. *Journal of Geophysical Research*, 88(C3), 1563–1571. <https://doi.org/10.1029/JC088iC03p01563>
- Hu, M., Li, J., Li, H., & Xing, L. (2014). Bathymetry predicted from vertical gravity gradient anomalies and ship soundings. *Geodesy and Geodynamics*, 5, 41–46. <https://doi.org/10.3724/SPJ.1246.2014.01041>
- Ingber, L. (1989). Very fast simulated re-annealing. *Mathematical and Computer Modelling*, 12(8), 967–973. [https://doi.org/10.1016/0895-7177\(89\)90202-1](https://doi.org/10.1016/0895-7177(89)90202-1)
- Ingber, L., & Rosen, B. (1992). Genetic algorithms and very fast simulated reannealing—A comparison. *Mathematical and Computer Modelling*, 16(11), 87–100. [https://doi.org/10.1016/0895-7177\(92\)90108-w](https://doi.org/10.1016/0895-7177(92)90108-w)
- Jakobsson, M. (2017). What will science gain from mapping the world ocean floor? In *Abstract OS14B-01 presented at 2017 Fall Meeting, AGU*, New Orleans, LA. <http://adsabs.harvard.edu/abs/2017AGUFMOS14B.01J>
- Jakobsson, M., Mayer, L., Coakley, B., Dowdeswell, J. A., Forbes, S., Fridman, B., et al. (2012). The International Bathymetric Chart of the Arctic Ocean (IBCAO) Version 3.0. *Geophysical Research Letters*, 39, L12609. <https://doi.org/10.1029/2012GL052219>
- Jekeli, C. (2013). Extent and resolution requirements for the residual terrain effect in gravity gradiometry. *Geophysical Journal International*, 195, 211–221. <https://doi.org/10.1093/gji/ggt246>
- Jekeli, C. (2017). *Spectral methods in geodesy and geophysics*. Boca Raton, FL: CRC Press.
- Kirkpatrick, S., Gelatt, C. D., & Vecchi, M. P. (1983). Optimization by simulated annealing. *Science*, 220(4598), 671–680. <https://doi.org/10.1126/science.220.4598.671>
- Laarhoven, P. J. M., & Aarts, E. H. L. (1987). *Simulated annealing: Theory and applications*. Dordrecht, Netherlands: Springer Science+Business Media. [https://doi.org/10.1007/978-94-015-7744-1\\_2](https://doi.org/10.1007/978-94-015-7744-1_2)
- Lewis, B. T., & Dorman, L. M. (1970). Experimental isostasy: 2. An isostatic model for the USA derived from gravity and topographic data. *Journal of Geophysical Research*, 75(17), 3367–3386. <https://doi.org/10.1029/JB075i017p03367>
- Marks, K. M., & Smith, W. H. F. (2006). An evaluation of publicly available global bathymetry grids. *Marine Geophysical Research*, 27, 19–34. <https://doi.org/10.1007/s11001-005-2095-4>
- Marks, K. M., & Smith, W. H. F. (2012). Radially symmetric coherence between satellite gravity and multibeam bathymetry grids. *Marine Geophysical Research*, 33, 223–227. <https://doi.org/10.1007/s11001-012-9157-1>
- Marks, K. M., Smith, W. H. F., & Sandwell, D. T. (2010). Evolution of errors in the altimetric bathymetry model used by Google Earth and GEBCO. *Marine Geophysical Research*, 31, 223–238. <https://doi.org/10.1007/s11001-010-9102-0>
- McKenzie, D. P., & Bowin, C. (1976). The relationship between bathymetry and gravity in the Atlantic Ocean. *Journal of Geophysical Research*, 81(11), 1903–1915. <https://doi.org/10.1029/JB081i011p01903>
- McNutt, M. (1979). Compensation of oceanic topography: An application of the response function technique to the surveyor area. *Journal of Geophysical Research*, 84(B13), 7589–7598. <https://doi.org/10.1029/JB084iB13p07589>
- Metropolis, N., Rosenbluth, A. W., Rosenbluth, M. N., Teller, A. H., & Teller, E. (1953). Equation of state calculations by fast computing machines. *The Journal of Chemical Physics*, 21(6), 1087–1092. <https://doi.org/10.1063/1.1699114>
- Parker, R. L. (1972). The rapid calculation of potential anomalies. *Geophysical Journal of the Royal Astronomical Society*, 31(4), 447–455. <https://doi.org/10.1111/j.1365-246X.1973.tb06513.x>
- Raittinen, H., & Kaski, K. (1990). Image deconvolution with simulated annealing method. *Physica Scripta*, 1990(T33), 126–130. <https://doi.org/10.1088/0031-8949/1990/T33/022>
- Ribe, N. M. (1982). On the interpretation of frequency response functions for oceanic gravity and bathymetry. *Geophysical Journal of the Royal Astronomical Society*, 70(2), 273–294. <https://doi.org/10.1111/j.1365-246X.1982.tb04968.x>
- Roy, L., Sen, M. K., Blankenship, D. D., Stoffa, P. L., & Richter, T. G. (2005). Inversion and uncertainty estimation of gravity data using simulated annealing: An application over Lake Vostok, East Antarctica. *Geophysics*, 70, J1–J12. <https://doi.org/10.1190/1.1852777>
- Rummel, R., & Haagmans, R. H. N. (1990). Gravity gradients from satellite altimetry. *Marine Geodesy*, 14(1), 1–12. <https://doi.org/10.1080/15210609009379641>
- Sailor, R. V., & Okal, E. A. (1983). Applications of Seasat altimeter data in seismotectonic studies of the South-Central Pacific. *Journal of Geophysical Research*, 88(NC3), 1572–1580. <https://doi.org/10.1029/JC088iC03p01572>
- Sandwell, D. T., Müller, R. D., Smith, W. H. F., Garcia, E., & Francis, R. (2014). New global marine gravity model from CryoSat-2 and Jason-1 reveals buried tectonic structure. *Science*, 346, 65–67. <https://doi.org/10.1126/science.1258213>
- Sandwell, D. T., & Smith, W. H. F. (1992). Global marine gravity from ERS-1, Geosat and Seasat reveals new tectonic fabric. *Eos, Transactions of the American Geophysical Union*, 73(43), 133. <https://doi.org/10.1029/91EO10347>
- Sandwell, D. T., & Smith, W. H. F. (1997). Marine gravity anomaly from Geosat and ERS 1 satellite altimetry. *Journal of Geophysical Research*, 102(B5), 10,039–10,054. <https://doi.org/10.1029/96JB03223>
- Sandwell, D. T., Smith, W. H. F., Gille, S., Kappel, E., Jayne, S., Soofi, K., et al. (2006). Bathymetry from space: Rationale and requirements for a new, high-resolution altimetric mission. *Comptes Rendus Geoscience*, 338, 1049–1062. <https://doi.org/10.1016/j.crte.2006.05.014>
- Smith, W. H. F. (1993). On the accuracy of digital bathymetric data. *Journal of Geophysical Research*, 98(B6), 9591–9603. <https://doi.org/10.1029/93JB00716>
- Smith, W. H. F., & Marks, K. M. (2014). Seafloor in the Malaysia airlines flight MH370 search area. *Eos, Transactions of the American Geophysical Union*, 95, 173–174. <https://doi.org/10.1002/2014EO210001>
- Smith, W. H. F., & Sandwell, D. T. (1994). Bathymetric prediction from dense satellite altimetry and sparse shipboard bathymetry. *Journal of Geophysical Research*, 99(B11), 21,803–21,824. <https://doi.org/10.1029/94JB00988>

- Smith, W. H. F., & Sandwell, D. T. (1997). Global sea floor topography from satellite altimetry and ship depth soundings. *Science*, 277(5334), 1956–1962. <https://doi.org/10.1126/science.277.5334.1956>
- Smith, W. H. F., & Sandwell, D. T. (2004). Conventional bathymetry, bathymetry from space, and geodetic altimetry. *Oceanography*, 17, 8–23. <https://doi.org/10.5670/oceanog.2004.63>
- Smith, D. E., Zuber, M. T., Frey, H. V., Garvin, J. B., Head, J. W., Muhleman, D. O., et al. (2001). Mars orbiter laser altimeter: Experiment summary after the first year of global mapping of Mars. *Journal of Geophysical Research*, 106(E10), 23,689–23,722. <https://doi.org/10.1029/2000JE001364>
- Szu, H., & Hartley, R. (1987). Fast simulated annealing. *Physics Letters A*, 122(3), 157–162. [https://doi.org/10.1016/0375-9601\(87\)90796-1](https://doi.org/10.1016/0375-9601(87)90796-1)
- Uzun, S. (2013). *Estimating parameters of subsurface structures from airborne gravity gradiometry data using a Monte-Carlo optimization method*. Columbus, OH: School of Earth Sciences, The Ohio State University. Retrieved from <https://earthsciences.osu.edu/sites/earthsciences.osu.edu/files/report-506.pdf>
- Watts, A. B. (1978). An analysis of isostasy in the world's oceans 1. Hawaiian-Emperor seamount chain. *Journal of Geophysical Research*, 83(B12), 5989–6004. <https://doi.org/10.1029/JB083iB12p05989>
- Weatherall, P., Marks, K. M., Jakobsson, M., Schmitt, T., Tani, S., Arndt, J. E., et al. (2015). A new digital bathymetric model of the world's oceans. *Earth and Space Science*, 2, 331–345. <https://doi.org/10.1002/2015EA000107>
- White, J. V., Sailor, R. V., Lazarewicz, A. R., & Leschack, A. R. (1983). Detection of seamount signatures in Seasat altimeter data using matched filters. *Journal of Geophysical Research*, 88(NC3), 1541–1551. <https://doi.org/10.1029/JC088iC03p01541>
- Wieczorek, M. A. (2015). Gravity and topography of the terrestrial planets. In G. Schubert (Ed.), *Treatise on geophysics* (2nd ed., pp. 153–193). Oxford, UK: Elsevier. <https://doi.org/10.1016/B978-0-444-53802-4.00169-X>
- Yang, J. (2017). *Seafloor topography estimation from gravity gradients*. Columbus, OH: School of Earth Sciences, The Ohio State University. Retrieved from [http://rave.ohiolink.edu/etdc/view?acc\\_num=osu1512048462472145](http://rave.ohiolink.edu/etdc/view?acc_num=osu1512048462472145)
- Zhu, L. (2007). *Gradient modeling with gravity and DEM*. Columbus, OH: School of Earth Sciences, The Ohio State University. Retrieved from <https://earthsciences.osu.edu/sites/earthsciences.osu.edu/files/report-483.pdf>